Supporting information

Simple and efficient synthesis methods for fabricating anode materials of sodium-ion batteries and their sodium-ion storage mechanism study

Pan Zhang[1,2], Yirui Shu[1,2], Ye Wang[1,2], Jinghua Ye[1,2] and Lin Yang*[12]

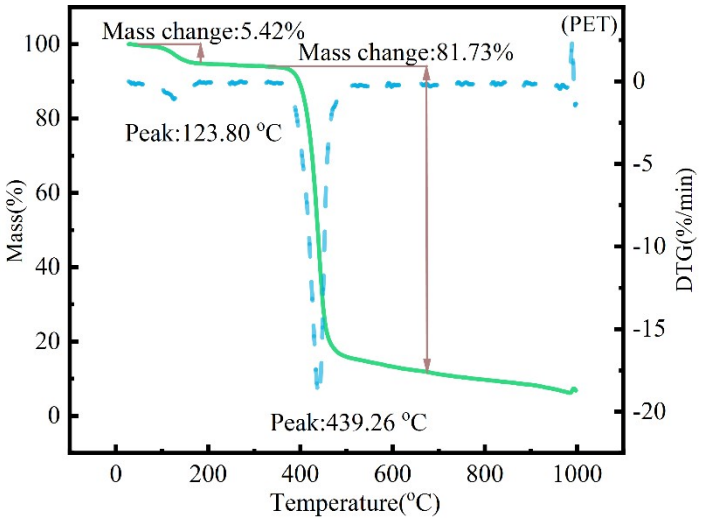

Fig.S1 TG analysis of the PET raw material.

1. Chemical Science and Engineering College, Sichuan University, Chengdu 610065, China, P R

2. Engineering Research Center of Comprehensive Utilization and Clean Processing of Phosphorus，Chengdu 610065, China, P R

*Corresponding author: Lin Yang; TEL: +862885405201; E-mail: 18980632893@163.com

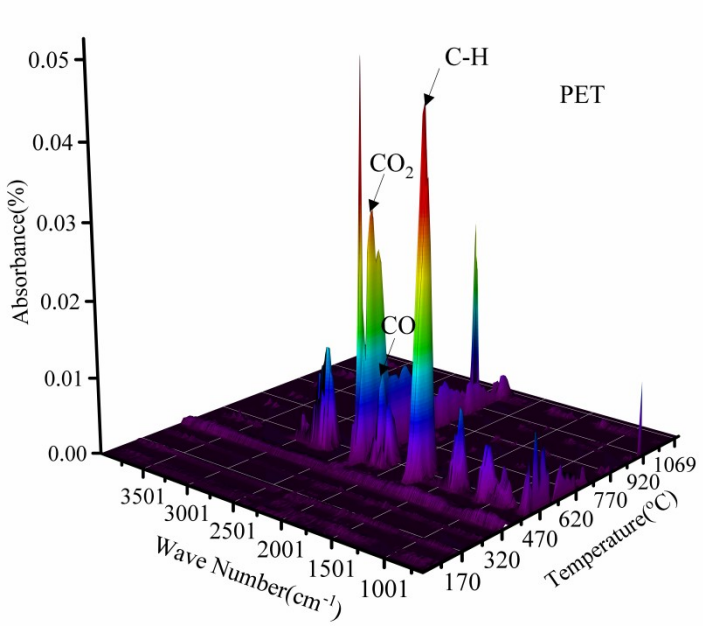

Fig.S2 FTIR analysis of the PET raw material .

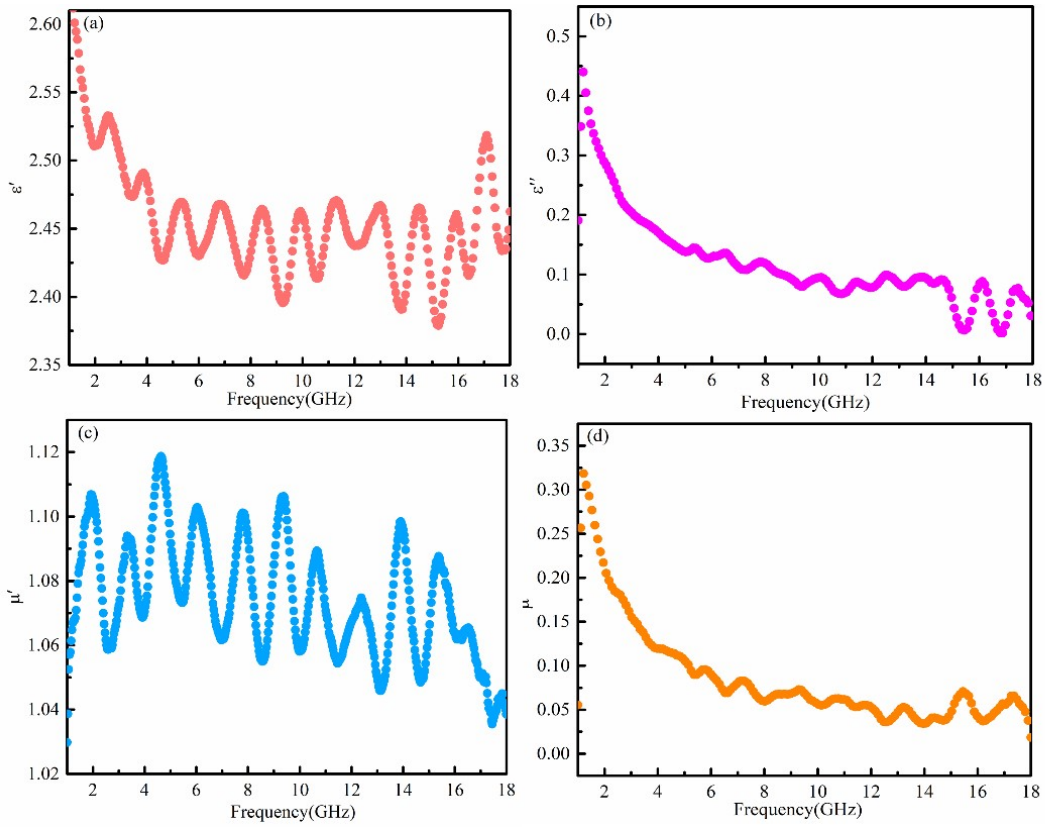

Fig.S3 Electromagnetic paremeters of PET:(a)Real pa(ε′) and (b)imaginary part(ε″) of the complex permittivity;(c)Real part(μ′);(d)imaginary part(μ″)of the permeability.

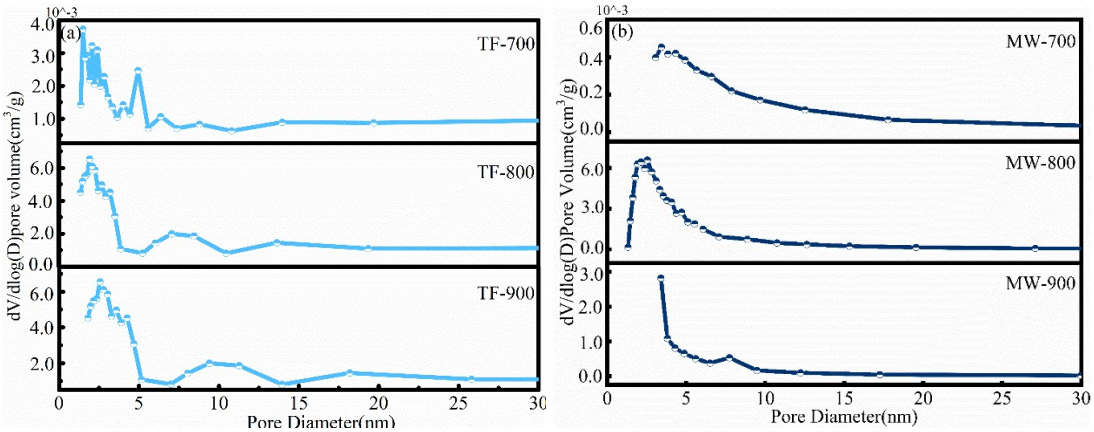

Fig.S4 The corresponding pore size distributions of TF-HC(a),and MW-HC(b).

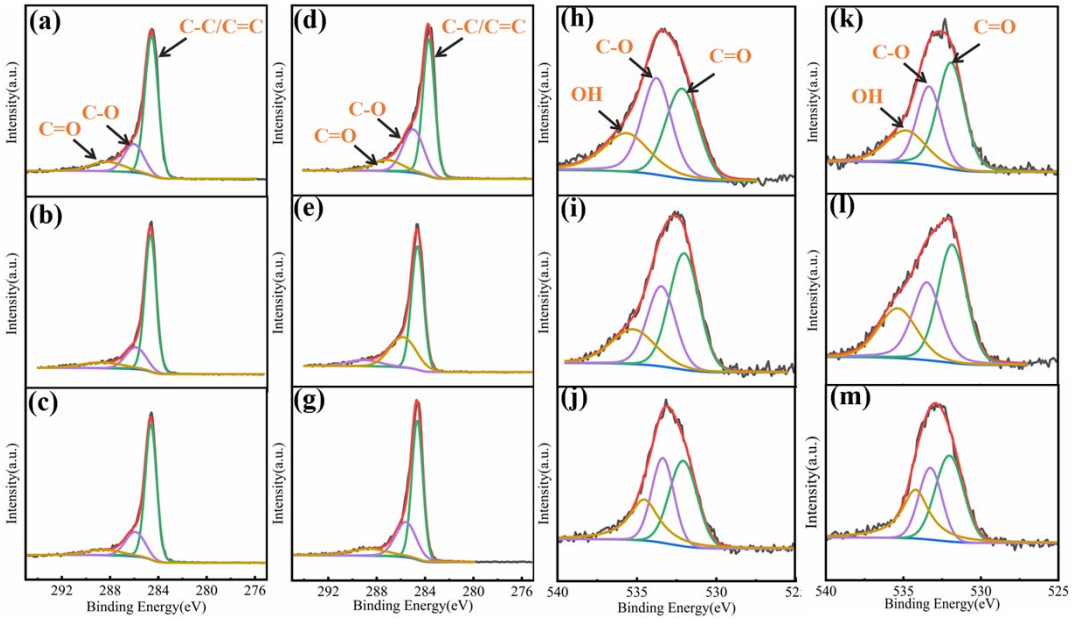

Fig.S5 XPS of spectra of TF-HC and MW-HC at different temperatures:(a-g) C 1s peak of TF-700, TF-800, TF-900 and MW-700, MW-800,MW-900; (h-m) O 1s peak of TF-700, TF-800, TF-900 and MW-700, MW-800, MW-900.

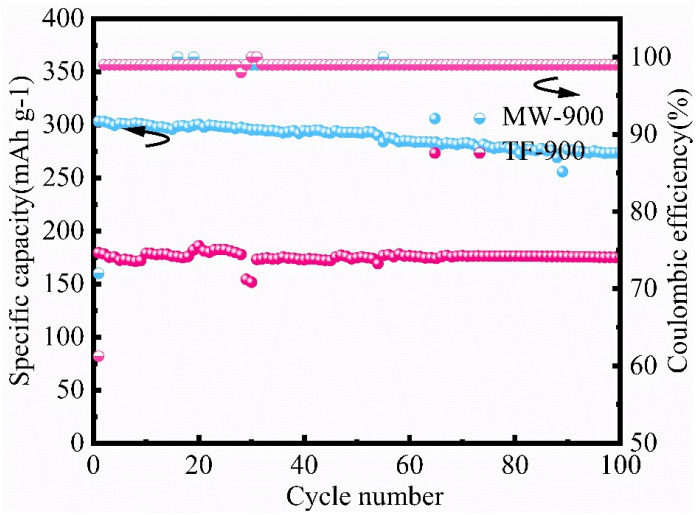

Fig.S6 Cycling performance of TF-900 and MW-900

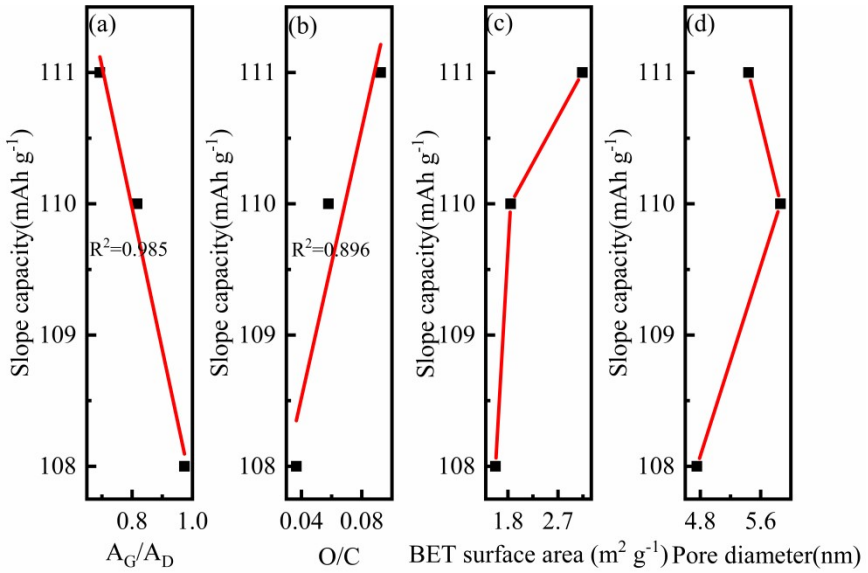

Fig.S7 Relation curves of the slope capacities of TF-HC(TF-700、TF-800、TF-900): (a) the A_G/A_D ratios from the previous Raman spectra, (b) the atomic ratios of oxygen over carbon from the previous XPS spectra, (c) the BET surface areas, (d) the pore diameter from the previous BET tests. it can be seen that the open pores may improve the adsorption of Na^+.

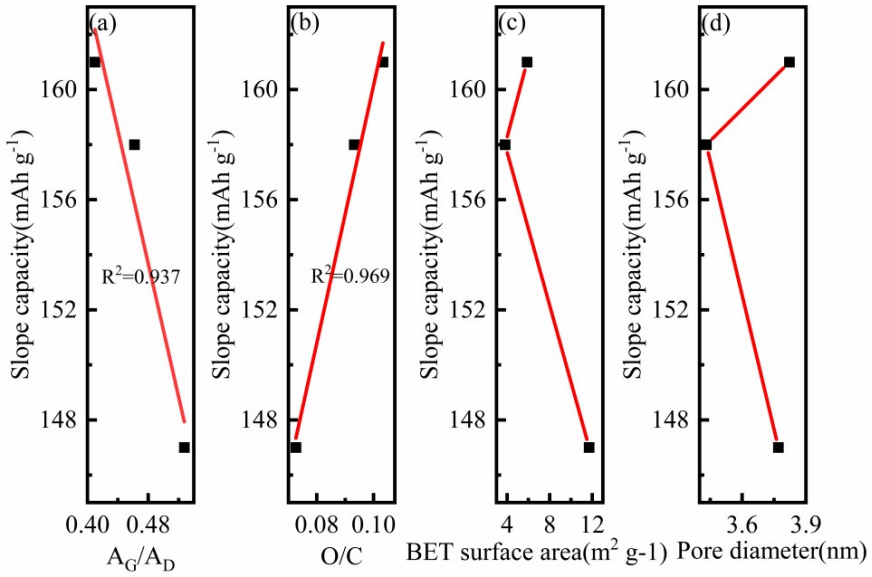

Fig.S8 Relation curves of the slope capacities of MW-HC (MW-700、MW-800、MW-900): (a) the A_G/A_D ratios from the previous Raman spectra, (b) the atomic ratios of oxygen over carbon from the previous XPS spectra, (c) the BET surface areas, (d) the pore diameter from the previous BET tests.

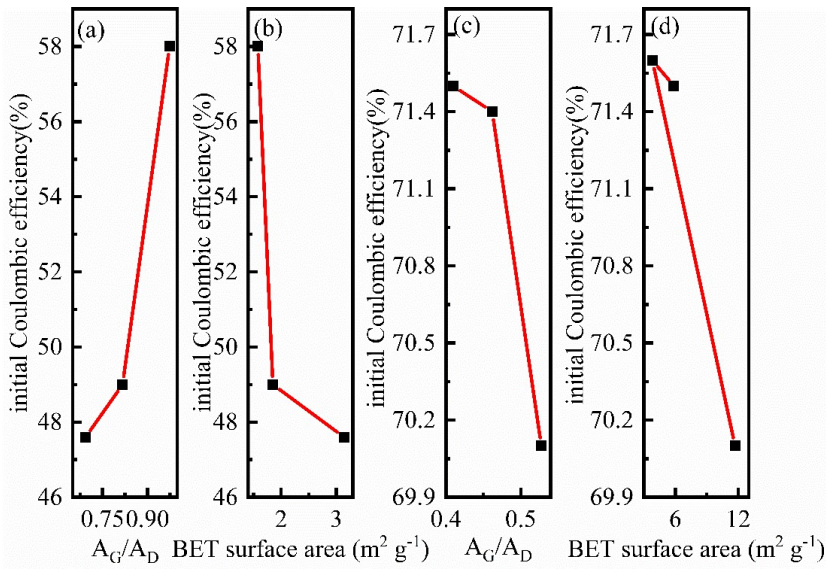

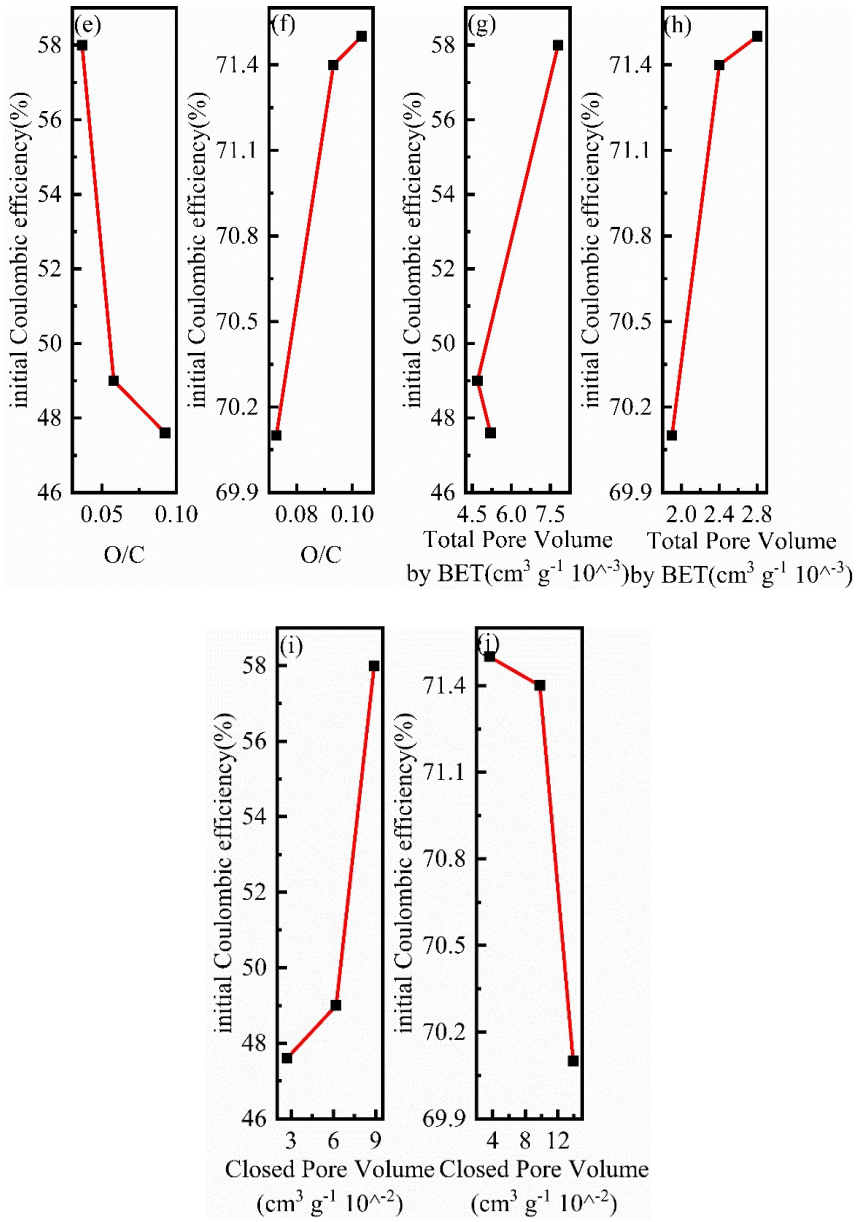

Fig.S9. Relation curve of ICEs and (a)A_G/A_D from the TF-HC and (b) BET surface areas for the TF-HC, (c)A_G/A_D for the MW-HC and (d) BET surface areas for the MW-HC, (e) the atomic ratios of oxygen over carbon for the TF-HC, (f) the atomic ratios of oxygen over carbon for the MW-HC, (g) open pore volume for TF-HC, (h) open pore volume for MW-HC, (i) closed pore volume for TF-HC, (j) closed pore volume for MW-HC.

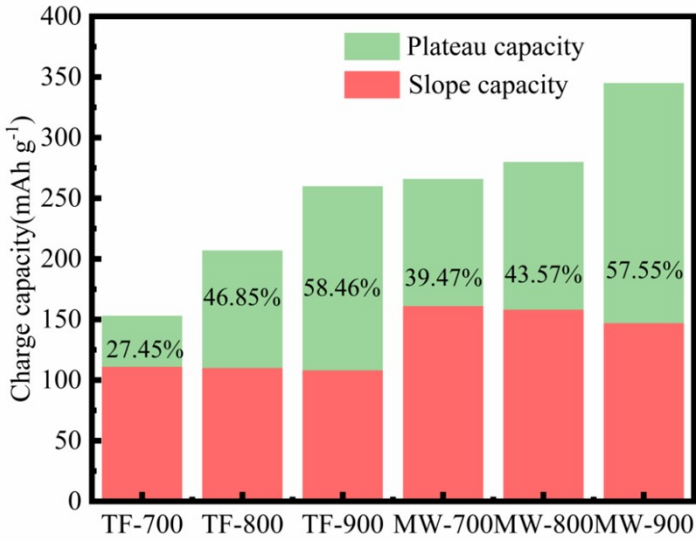

Fig.S10. Percentage of capacities in sloping and plateau regions for TF-HC and MW-HC

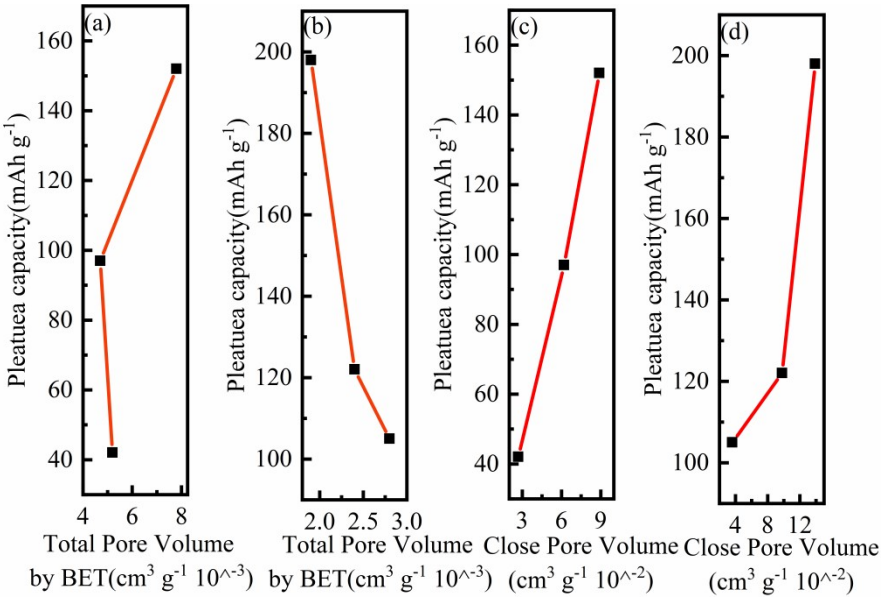

Fig.S11. Relation of open pore volume to plateau zone:(a) TF-HC, (b) MW-HC; Relation of closed pore volume to plateau zone: (c) TF-HC, (d) MW-HC.

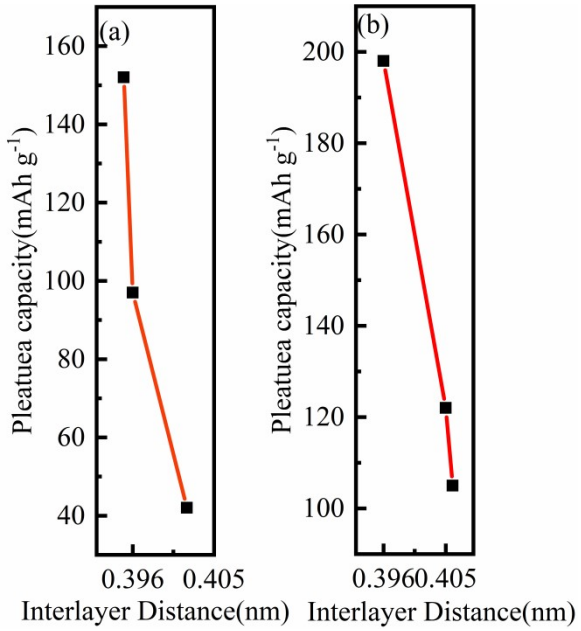

Fig.S12. Relationship between layer spacing and platform capacity for TF-HC and MW-HC

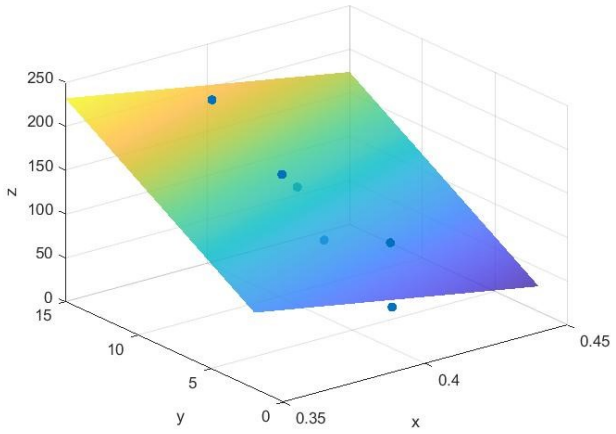

Fig.13. Coupling diagram of obturator and carbon layer spacing with plateau capacity

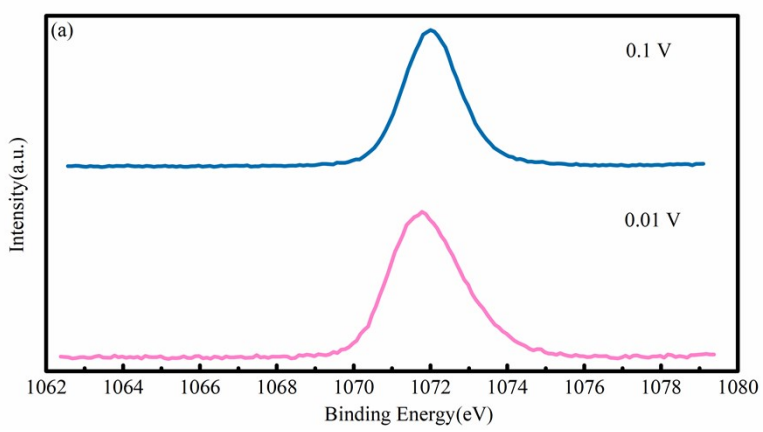

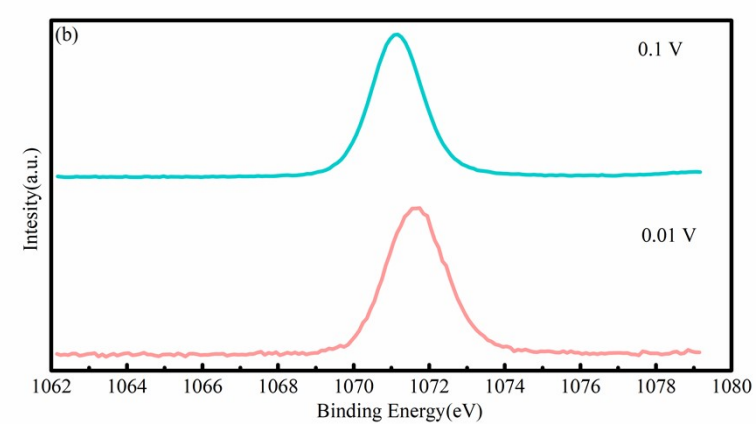

Fig.S14. Ex-situ XPS Na 1s spectra of a) TF-900, b) and MW-900 at different discharged states

Table-S1 Summary of data gleaned from the Raman spectra of MW-HC and TF-HC at different temperatures

Sample	C_{cr}(%)	C_{am}(%)	A_{D1}/A_G
MW-700	61.32	38.68	2.44
MW-800	60.13	39.87	2.165
MW-900	66.26	33.73	1.896
TF-700	75.53	24.47	1.427
TF-800	76.19	20.81	1.262
TF-900	77.54	22.46	0.998

Table-S2 Comparison among previous reported porous carbon electrodes for NIBs

Reference	Calcination temperature (°C)	Open pore information (N_2 adsorption/desorption)	Reversible capacity	Ref.
This work	900	SBET:12.1m^2g^{-1};Vopen pores:0.0019 cm^3g^{-1}	344 mAh g^{-1}@20mA g^{-1}@70.1%	/
Furfuryl alcohol derived spherical carbon	1150	SBET:480 m^2g^{-1};Vopen pores:0.164 cm^3g^{-1}	223 mAh g^{-1}@20mA g^{-1}@67.3%	1
Argan shells derived hard carbon	1300	SBET:24 m^2g^{-1} Vopen pores:0.18 cm^3g^{-1}	333 mAh g^{-1}@25mA g^{-1}@67.8%	2

Lotus seedpod	1200	SBET:14.7 m^2g^{-1} Vopen pores: 0.22 $cm^3\ g^{-1}$	328 mAh g^{-1} @50 mA g^{-1}@50.4%	3
Sorghum stalk	1300	SBET: 85.5 $m^2\ g^{-1}$	245 mAh g^{-1} @25mA g^{-1}@62.2%	4
Poly(styrene) latexes-glucose derived hollow nanospheres	1100	SBET:410 $m^2\ g^{-1}$	223 mAh g^{-1} @50mA g^{-1}@41.5%	5
Cherry petals	1000	SBET:1.86 $m^2\ g^{-1}$	310 mAh g^{-1} @20mA g^{-1}@67.3%	6

Table-S3 Summary of data from the TF-900-CT and TF-900

Slope capacity (mAh g^{-1})	Plateau capacity (mAh g^{-1})	Ture density (He) (g cm^{-3})	Vclosed pore ($cm^3\ g^{-1}$)
150	166	1.79	0.116
151	109	1.88	0.089

Eq.S1 The calculation formula is as follows:

$$D = \frac{4}{\pi\tau}\left(\frac{m_B V_M}{M_B S}\right)^2 \frac{\Delta E_s}{\Delta E_\tau}$$

where τ (sec) is the pulse time, S is the active surface area (cm^2), m_B(g), M_B(g/mol) and V_M (cm^3 /mol) are the mass, molar mass and molar volume of CCs. ΛE_s (V) and ΔE_τ (V) are voltage change caused by current pulse and galvanostatic discharge.

References (supporting information)

[1]Zhou D. H., Peer M., Yang Z. Z., Pol V. G. Long cycle life microporous spherical carbon anodes for sodium-ion batteries derived from furfuryl alcohol. Journal of Materials Chemistry A. 17(2016)6271-6275.

[2]Xie F., Xu Z., Jensen A. C. S., Ding F. Unveiling the role of hydrothermal carbon dots as anodes in sodium-ion batteries with ultrahigh initial coulombic efficiency. Journal of Materials Chemistry A. 48(2019)27567-27575.

[3]Dahbi M., Kiso M., Kubota K., Horiba T. Synthesis of hard carbon from argan shells for Na-ion batteries. Journal of Materials Chemistry A. 20(2017)9917-9928.

[4]Wu F., Zhang M., Bai Y., Wang X. Lotus Seedpod-Derived hard carbon with hierarchical porous structure as stable anode for sodium-ion batteries. ACS Applied Materials & Interfaces. 13(2019)12554-12561.

[5]Zhu X., Jiang X., Liu X., Xiao L. A green route to synthesize low-cost and high-performance hard carbon as promising sodium-ion battery anodes from sorghum stalk waste. Green Energy & Environment. 3(2017)310-315.

[6]Zhu Z., Liang F., Zhou Z., Zeng X. Expanded biomass-derived hard carbon with ultrastable performance in sodium-ion batteries. Journal of Materials Chemistry A. 4(2018) 1513-1522.